PERGAMON

Scripta mater. 44 (2001) 2055–2059

Scripta MATERIALIA

www.elsevier.com/locate/scriptamat

APPLICATIONS OF NANOCOMPOSITES

B. Cantor*, C.M. Allen*, R. Dunin-Burkowski*, M.H. Green**, J.L. Hutchinson*, K.A.Q. O'Reilly*, A.K. Petford-Long*, P. Schumacher*, J. Sloan** and P.J. Warren*

*Department of Materials and **Department of Chemistry, Oxford University, Oxford, UK

(Received August 25, 2000)
(Accepted in revised form December 27, 2000)

Keywords: Magnetic multilayers; Devitrified amorphous alloys; Carbon nanotubes; Secondary phases; Grain refiners

1. Introduction

This paper considers examples of how a material nanostructure can influence its properties. The examples covered are grain refiners and secondary phases in commercial wrought Al alloys, devitrified amorphous magnetic Fe alloys, magnetic multilayers for storage media and read/write devices, and 1-D crystals in single walled C nanotubes.

2. Grain Refinement in Al Alloys

Wrought Al alloys are used in applications such as beverage cans, lithographic sheet and automotive panels. During casting, primary Al grain sizes must be $<100\mu$m to ensure isotropic properties. Grain refinement is achieved by adding TiB_2 and Al_3Ti in a master alloy, but the nucleation mechanism is not well understood. Neither TiB_2 nor Al_3Ti work alone. TiB_2 is stable in liquid Al, but does not react to form solid Al; Al_3Ti reacts peritectically but is not stable at grain refinement addition levels (1). Observing nucleation is difficult, as it is obscured by subsequent crystal growth. A glass forming alloy can be used as a slow motion analogue of an undercooled liquid, allowing TEM study of the nucleation mechanism. Fig 1 shows a TEM image of a $<100>$ hexagonal TiB_2 plate viewed edge-on along its basal plane. The particle is embedded in amorphous $Al_{85}Ni_8Y_7Co_2$, with the basal faces covered by a few monolayers thick adsorbed Al_3Ti, which has nucleated crystals of Al. The fcc Al crystals, tetragonal DO_{22} Al_3Ti layer and hexagonal TiB_2 plate have close-packed directions and planes parallel, with the pseudo close-packed (112) planes in the thin Al_3Ti layer stretched to match TiB_2, giving large strains in the nucleated Al. The 2–5nm Al crystal size is much smaller than in undercooled Al melts, where the critical nucleus size is -1m at 0.5K undercooling. Mismatch dislocations are required to maintain coherency in Al crystals larger than 5nm.

3. Secondary Phases in Al Alloys

Ppm impurity levels in wrought Al alloys influence the formation of nm-scale aluminide secondary phases, which control final properties such as surface finish, corrosion and strength. These effects are

PII: S1359-6462(01)00891-0

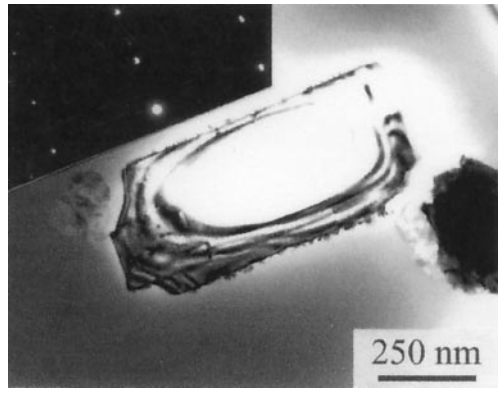

Figure 1. TEM image of a <100> hexagonal TiB_2 plate viewed edge-on along its basal plane, with the basal faces covered by a few monolayers thick adsorbed Al_3Ti, which has nucleated crystals of Al.

difficult to study at low concentrations, with initial aluminide formation swamped by subsequent growth. Rapid solidification followed by heat treatment in the mushy zone produces $>10^{15}m^{-3}$ solute rich 10–100nm sized droplets in a solid Al alloy matrix. On re-cooling, $>10^{15}m^{-3}$ aluminide particles solidify simultaneously, and the cumulative effect can be monitored calorimetrically. Microscopy can then be used to identify the nucleation mechanism (2). Fig 2 shows a FEGSEM image of the internal structure of a quenched 100nm sized droplet in an Al-0.3wt%Fe-0.1wt%Si-0.05wt%V alloy. On slow cooling the droplets form Al-$FeAl_m$ eutectic, which is responsible for degradation of surface quality in anodising Al sheet.

4. Devitrification of Amorphous Alloys

Primary crystallization of an amorphous alloy often results in a nanocrystalline structure with excellent magnetic (3–5) or mechanical (6,7) properties, with potential industrial applications. 3-D atom probe (3DAP) can be used to determine local compositions in nanocrystalline materials. Atoms are field evaporated and identified by mass spectrometry (8), with typical collection rates of 10^6/day from a volume of $-20 \times 20 \times 100$nm. 3DAP of soft magnetic nanocrystalline $Fe_{71.5}Si_{13.5}B_9Nb_3Cu_1Al_2$ shows

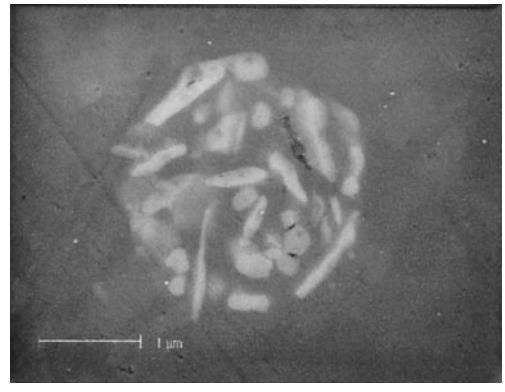

Figure 2. FEGSEM image of the internal structure of a quenched 100nm sized droplet in an Al-0.3wt%Fe-0.1wt%Si-0.05wt%V alloy.

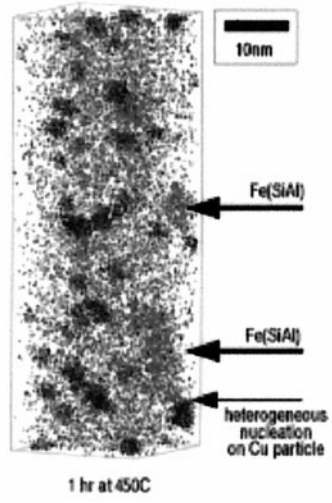

Figure 3. Atom map of Fe(Si, Al) nanocrystals nucleated heterogeneously on Cu clusters in a Nb and B rich amorphous matrix.

that Al partitions into ∀-Fe(Si), decreasing its magnetic anisotropy. Al is also incorporated into the Cu clusters which control the initial crystallization by nucleating nm-scale Fe(Si) particles (9,10). Fig 3 shows the Al and Cu atoms in a 20 × 20 × 60nm volume. Al atoms are partitioned into Fe(Si,Al) nanocrystals which are nucleating on the Cu clusters. 3DAP also shows partitioning behaviour in hard magnetic nanocrystalline Pr(FeCo)B. Co increases grain size and therefore Curie temperature in 2 phase $Pr_2Fe_{14}B_1$-Fe alloys (11), but partitions differently from Nd in the corresponding Nd alloys. Co is distributed uniformly, enhancing the Co:Fe ratio in $Pr_2(Fe,Co)_{14}B_1$ compared to the single phase alloy and increasing the Curie temperature.

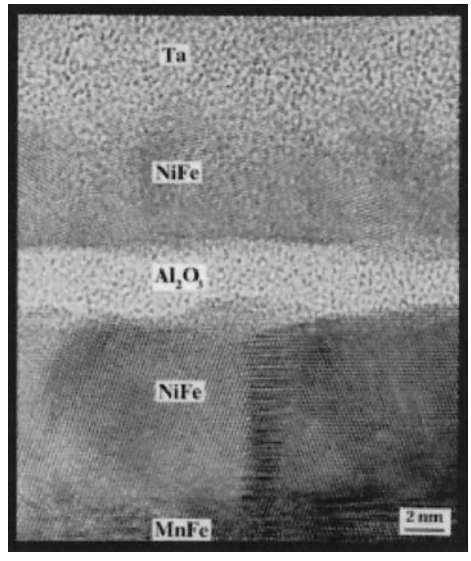

Figure 4. Cross-section HREM image through a MnFe/NiFe/Al_2O_3/NiFe/Ta spin-tunnel junction.

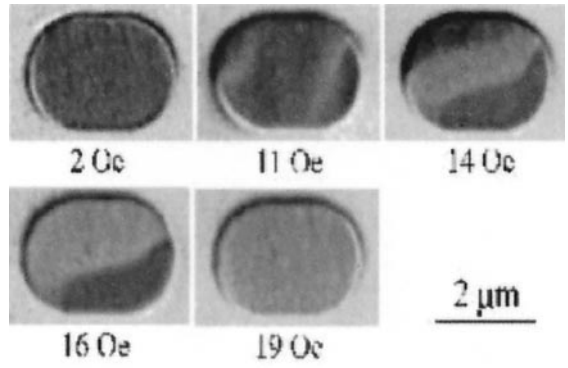

Figure 5. Lorentz TEM images of a spin-tunnel junction during reversal of the magnetisation of the free layer. Dark and light contrast regions are magnetic domains.

5. Magnetic Multilayers

Since GMR was reported in magnetic layered films, rapid progress has led to useful device structures. The most successful structures for read heads and non-volatile memories are spin valves (SVs), in which resistance changes by 8–20% in an applied magnetic field of a few Oe (12,13). In an SV, 2 ferromagnetic (FM) layers are separated by a metal spacer layer, with magnetisation in one FM layer pinned by an antiferromagnetic layer. Magnetisation in the other FM layer can rotate in a magnetic field. If the metal layer is replaced by an insulator and current is passed through the layers, it is called a spin tunnel junction (STJ). Fig 4 shows an HREM image of a sputter deposited STJ (grown by Hewlett-Packard Labs). The amorphous alumina spacer layer has a pale random contrast. The interfaces between the layers are not flat, and this affects the device response. The resistance change caused by the diferent

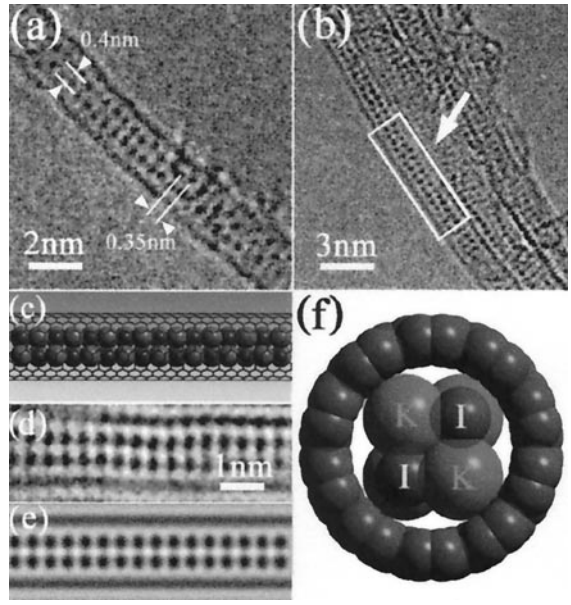

Figure 6. (a) and (b) HREM image of 2 × 2 atom thick KI crystal chain in single wall C nanotube; (c)–(e) atomistic model, HREM image and image simulation of section of KI crystal chain; and (f) end-on projection.

relative orientations of magnetisation in the 2 FM layers change allows 1 or 0 to be stored in each memory element or bit. The mechanism of magnetisation reversal is important, particularly when the material is patterned lithographically into small elements. Fig 5 shows Lorentz TEM images of magnetisation reversal in an STJ in an in-situ applied magnetic field.

6. Carbon Nanotubes

C nanotubes can be filled with different materials, leading to 1-D crystallization of salts within the confining nanotube walls. The typical nanotube internal diameter is −1nm. We have found: twisted chains of $CdCl_2$, a polyhedral chain structure with unusual cation coordination (14); the high pressure rocksalt structure in halides such as CsCl (15); and tetragonal distortions in halides such as KI, grown as 2 or 3 atom wide chains, ie sub-unit cell crystals with all atoms at the surface (16). Fig 6 shows an example of a 2 atom wide KI crystal chain in a single walled C nanotube. Image reconstruction (16) generates phase images with aberration corrected atomic positions to better than 0.01nm accuracy.

Acknowledgments

EPSRC, Alcan, Hewlett-Packard Laboratories, Palo Alto, Department of Materials, Royal Society.

References

1. P. Schumacher, A. L. Greer, J. Worth, P. V. Evans, M. A. Kearns, P. Fisher and A. H. Green, Mater. Sci. & Techn., 14, 394 (1998).
2. C. M. Allen, K. A. Q. O'Reilly, P. V. Evans and B. Cantor, Acta Materialia, 47, 4387 (1999).
3. Y. Yoshizawa, S. Oguma, and K. Yamauchi, J. Appl. Phys. 64, 6044 (1988).
4. K. Suzuki, A. Makino, A. Inoue, and T. Masumoto, Sci. Rep. RITU. A39, 133 (1994).
5. S. Hirosawa, H. Kanekiyo, and M. Uehara, J. Appl. Phys. 73, 6488 (1993).
6. A. Inoue, Y. Oorio, Y. H. Kim, and T. Masumoto, Mater. Trans. JIM. 33, 669 (1992).
7. H. Chen, Y. He, G. J. Shiflet, and S. J. Poon, Scripta Metall. Mater. 25, 1421 (1991).
8. A. Cerezo, T. J. Godfrey, S. J. Sijbrandij, G. D. W. Smith, and P. J. Warren, Rev. Sci. I. 69, 49 (1998).
9. P. J. Warren, I. Todd, H. A. Davies, A. Cerezo, M. R. J. Gibbs, D. Kendall, and R. V. Major, Scripta Mater. 41, 1223 (1999).
10. K. Hono and D. H. Ping, Mater. Charact. 44, 203 (2000).
11. C. L. Harland and H. A. Davies, J. Appl. Phys. in press.
12. J. C. S. Kools, IEEE Trans. Mag. 32(4), 3165 (1996).
13. J. S. Moodera and G. Mathon, J. Magn. Magn. Mater. 200, 248 (1999).
14. J. L. Hutchison, JEOL News. 34E, 10 (1999).
15. J. Sloan, Chem. Phys. Lett. in press.
16. R. Meyer, Science. in press.